Numerical and experimental investigation of utilizing the porous media model for windbreaks CFD simulation

Ahmed Osama Mahgoub *, Saud Ghani

Department of Mechanical and Industrial Engineering, Qatar University, P.O. Box 2713, Doha, Qatar

ARTICLE INFO

ABSTRACT

Windbreaks such as vegetation barriers, fences, and buildings' perforated facades are used in various environmental and wind mitigation applications. Numerical simulation of the airflow through windbreaks is challenging as modeling of the exact geometry needs large computational power. The computational cost can be reduced by modeling the windbreaks using the porous media model. The computational fluid dynamics (CFD) model uses empirical coefficients that need to be determined experimentally. This research develops empirical formulae to determine the needed viscous and inertial loss coefficients as a function of porosity for perforated windbreaks. Particle image velocimetry (PIV) experiments and pressure measurements were performed in a wind tunnel for scaled windbreaks models of porosity ratios ranging from 0.25 to 0.6. CFD simulations were carried out for the exact geometry and for the approximated numerical model. The CFD results of both models were compared against the experimental results. Hence, a correlation between the windbreaks porosity and the needed coefficients to utilize the CFD porous media model was obtained. Compared to exact geometry CFD results, the average velocity and pressure drop values obtained from the porous media model yielded an average error of 10.5% and 12%, respectively.

1. Introduction

Windbreaks are used to control the environmental wind conditions within a space. They can control wind erosion, sand movement and deposition, micro-climate and soil conditions (Liu, Qu, Zhang, Tan, & Gao, 2014). Windbreaks can be natural, such as vegetation barriers, or industrial, such as perforated fences and buildings' facades.

Porous structures are used as barriers for wind, sand and snow. It can also be used as safety protection screens for heat exchangers (Ghani et al., 2018), screens in wind tunnels for controlling boundary layer separation, reducing turbulence intensity and ensuring flow uniformity (He, Zhang, Gao, Sun, & Huang, 2019), acoustic barriers (Soper, Gillmeier, Baker, Morgan, & Vojnovic, 2019), and as buildings' permeable cladding for thermal insulation and rain protection (Kemper & Feldmann, 2019). Porous structures can also be used to reduce drag in turbulent channel flows (Breugem, Boersma, & Uittenbogaard, 2006; Rosti, Brandt, & Pinelli, 2018). Fig. 1 shows examples of various natural and industrial porous elements used in different environmental applications.

The airflow through windbreaks depends on the incident flow properties such as wind incidence angle and wind speed, and geometrical parameters such as the fence height, thickness and porosity. The porosity ratio is one of the important geometrical properties of windbreaks, as it affects their performance (Dong, Luo, Qian, & Wang, 2007). Previous experimental and numerical studies focused on investigating windbreaks of different porosity ratios for performance comparison and selection of optimum configurations. Experimentally, as wind tunnels have limited test section space, a scaled down model is typically used. This often leads to scaling and modeling difficulties when dealing with complex geometries such as perforated windbreaks (Liu et al., 2014). Computational fluid dynamics (CFD) simulations can address the difficulty of model scaling. However, due to the complex geometry of windbreaks, simulation of the airflow past the exact perforated geometry often incurs high computational cost as a refined computational model of millions of grid cells is needed to produce viable results.

Porous media models offer an approximation alternative for reducing the computational cost of modeling the exact complex geometry of windbreaks. The complex exact geometry of the perforated structure can be simplified as a solid geometry of prescribed porosity factors. Substantially reducing the CFD model size. The effect of the presence of the porous barrier is modeled by modifying the

---

* Corresponding author.
E-mail addresses: ahmed.mahgoub@qu.edu.qa (A.O. Mahgoub), s.ghani@qu.edu.qa (S. Ghani).

Nomenclature

CFD	computational fluid dynamics
FB	fractional bias
MG	geometric mean bias
PIV	particle image velocimetry
PTV	particle tracking velocimetry
R	correlation coefficient
VG	geometric variance
b	perforated surface width (m)
C	inertial resistance matrix of perforated surface (m^{-1})
$C_{2,x}$	inertial resistance of perforated surface in x-direction (m^{-1})
C_p	pressure coefficient
d	hole diameter (m)
D	viscous resistance matrix of perforated surface (m^{-2})
h	perforated surface height (m)
k	turbulent kinetic energy (m^2/s^2)
l	distance between holes of the perforated surface (m)

p	pressure (Pa)
p_0	reference pressure (Pa)
Re	Reynolds number
S_{porous}	sink term of porous media model
t	perforated surface thickness (m)
$\boldsymbol{u}$	velocity vector (m/s)
U	velocity magnitude (m/s)
U_0	reference velocity (m/s)
u, v, w	x, y and z components of velocity field (m/s)
x, y, z	cartesian coordinates (m)
α, α_x	permeability of the perforated surface (m^2)
Δp	pressure drop (Pa)
ε	dissipation rate (m^2/s^3)
μ	dynamic viscosity coefficient (kg/m.s)
ν	kinematic viscosity coefficient (m^2/s)
ρ	density (kg/m^3)
ϕ	porosity ratio

Navier–Stokes equations that govern the fluid motion. A sink term that models the effect of the inertial and viscous resistances is added to the momentum equation. These terms rely on empirical coefficients that determine the different resistances in x, y and z directions.

1.1. Windbreaks and environmental barriers

Porous fences and vegetation barriers are used to reduce local pollutants particles concentration and to control the severity of high wind velocities in urban areas (Adamek, Vasan, Elshaer, English, & Bitsuamlak, 2017; Raupach, Woods, Dorr, Leys, & Cleugh, 2001). Earlier studies of wind barriers utilized experimental methods and empirical models. Currently, with the increase in computational power, researchers investigate the performance of windbreaks using numerical simulations.

Table 1 lists various studies investigating different configurations of windbreaks and environmental barriers. Different configurations, including vegetation barriers and porous fences were investigated
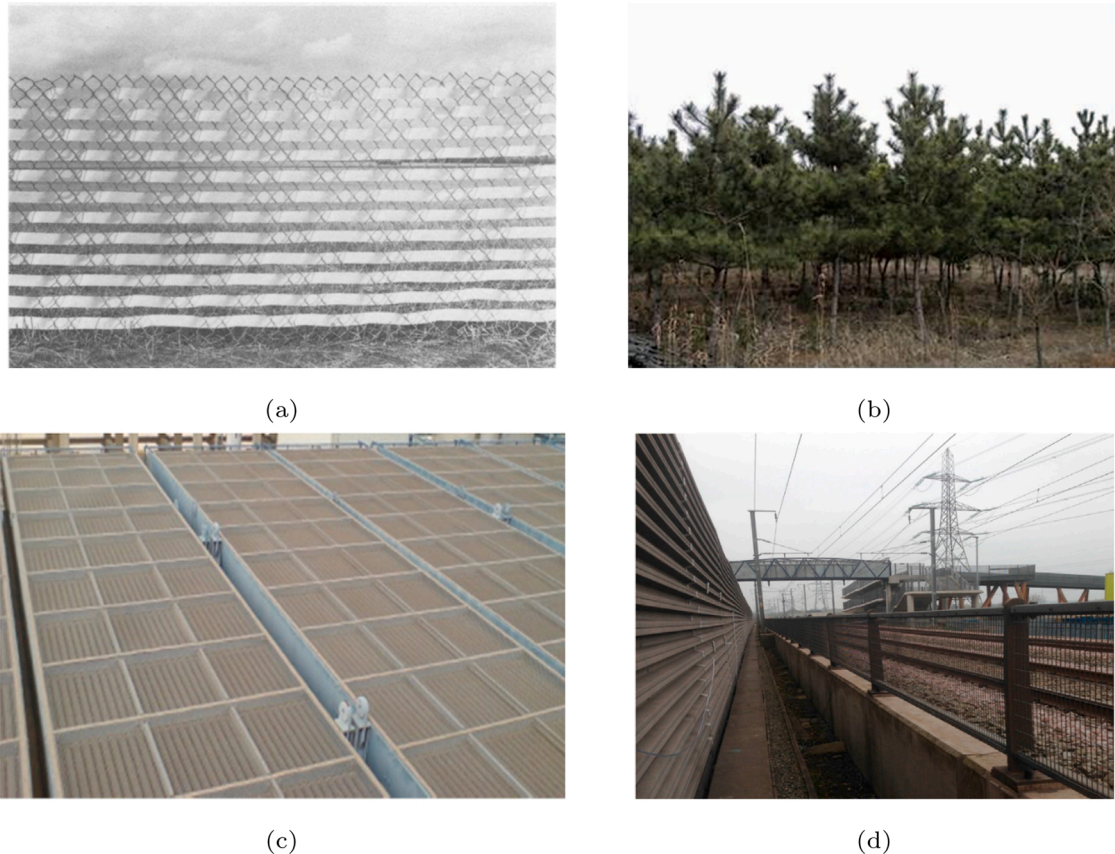

(a)

(b)

(c)

(d)

Fig. 1. Examples of various environmental barriers (a) porous windbreak fence (Wilson, 1987), (b) vegetation barrier acting as a windbreak (Bitog et al., 2011), (c) safety protection screen for heat exchangers (Ghani et al., 2018), and (d) acoustic barriers, (Soper et al., 2019).

Table 1
Literature on engineering applications of windbreaks.

Author – year	Conf.	Appl.	Method	Model	Porosity (ϕ)
Slinn (1982)	Veg. bar.	Particles barrier	Theo.	–	–
Wilson (1987)	Full-scale por. fen.	WB	Exp.	–	0.3–0.7
Wilson (1997)	Full-scale por. fen.	WB	Exp.	–	0.45
Lee and Kim (1999)	Por. fen.	WB	Exp.	–	0–0.65
Lee, Park, and Park (2002)	Por. fen.s	Sand barrier	Exp.	–	0–0.5
Dong et al. (2007)	Por. fen.	WB	Exp.	–	0.05–0.9
Procino, Kozmar, Bartoli, and Borsani (2008)	L-profile por. fen.	WB	Exp.	–	0.42
Kozmar, Procino, Bartoli, and Borsani (2009)	L-profile por. fen.	WB	Exp.	–	0.31–0.55
Dong, Luo, Qian, Lu, and Wang (2010)	Por. fen.	WB	Exp.	–	0.05–0.9
Dong et al. (2010)	Por. fen.	WB	Exp.	–	0.05–0.9
Bitog et al. (2011)	Veg. bar.	WB	Exp.	–	0.42–0.95
Cong, Cao, Chen, Peng, and Yang (2011)	Por. fen.	Particle barrier	Exp. &Num.	D&F	0.4
Raupach et al. (2001)	Veg. bar.s	Particles entrapment	Exp. &Theo.		–
Santiago, Martín, Cuerva, Bezdenejnykh, and Sanz-Andrés (2007)	Por. fen.	WB	Exp. &Num.	Δ P	0–0.5
Zheng et al. (2020)	Subtropical trees	WB	Exp. &Num.	Drag term	LAD
Patton, Shaw, and Judd (1998)	–	WB	Num.	Drag term	0.427
Hu, Yu, Chen, Li, and Liu (2012)	Urb. lay.	Urb. lay.	Num.	D&F	0.064–0.331
Guo, Hou, Yu, Li, and Guo (2013)	Por. fen.	Flow control	Num.	D&F	0.064–0.331
Nowak (2016)	Heat sink	Heat sink	Num.	D&F	–
Santiago et al. (2019)	Veg. bar.	Pollution reduction	Num.	Drag term	LAD
Kang, Kim, and Choi (2020)	Veg. bar.	Wind comfort	Num.	Drag term	LAD
Zeng et al., 2020	Veg. bar.	Wind comfort	Num.	Drag term	LAD

Conf. = Configuration, Veg. bar = Vegetation barrier, Por. fen. = Porous fence, Urb. lay. = Urban layout, Appl. = Application, WB = Wind barrier, Exp. = Experimental, Num. = Numerical, Emp. = Empirical model, Theo. = Theoretical, D&F = Darcy and Forchheimer model, ΔP = Pressure drop term.

experimentally and numerically. The applications are not limited to wind sheltering, but include protection against particles and pollution reduction. The trees porosity were defined using the leaf area density (LAD), which has a unit of m^2/m^3. Experimental methods include pressure measurement, particle image velocimetry (PIV) and particle tracking velocimetry (PTV). The methods are not limited to experimental tests, but also include empirical and analytical models.

Experimental tests are essential for assessing windbreaks performance. However, experimental results are susceptible to errors and inherited uncertainty. In particular, wind tunnel simulations are affected by the model scaling and wind tunnel testing section blockage. Additionally, it is challenging to physically scale down the exact porous geometry. For a scaled down windbreak model, not all of the flow characteristics are captured correctly (Liu et al., 2014). Thus, in order to eliminate the effect of scaling down, numerical simulations are needed. Table 1 shows the increased researchers' interest in using numerical simulations to evaluate the aerodynamic performance of porous fences and vegetation barriers.

1.2. Porous media model approximation

It is challenging to numerically model windbreaks, such as vegetation barriers and porous fences, as the exact model would require a large number of grid cells. Drawing the complex geometry of trees is a difficult and time consuming task. Moreover, exact geometry modeling can result in a model that cannot be solved (Zheng et al., 2020). Therefore, approximated methods for representing windbreaks and vegetation barriers, such as porous media models, are used. For numerical simulations of vegetation barriers, trees are usually drawn as cuboids having different heights and dimensions to represent trees of varying shapes. Additionally, a frontal area equal to that of the exact tree geometry can also be used (Bitog et al., 2011; Kang et al., 2020; Zheng et al., 2020). Wang, Takle, and Shen (2001) provided a review of modeling and numerical simulation studies of the airflow around shelter-belts and windbreaks comparing numerical simulations with experimental data. Buccolieri, Santiago, Rivas, and Sanchez (2018) reviewed the modeling techniques used for urban trees in CFD simulations. The review considered modeling the thermal effects of trees as well as their aerodynamic effect. Utilization of the porous media model is not limited to windbreaks, but it can be also utilized to simulate spectators sitting inside a stadium (Mahgoub, Ghani, Rashwan, Ismail, & ElBialy, 2020) and to represent crops inside a greenhouse Ghani et al. (2020). Porous media models can also be used for modeling forests and areas with vegetation (Bitog et al., 2011; Gromke, 2018; Kent, Grimmond, & Gatey, 2017).

The porous media model was extensively utilized in various studies. Darcy law was one of the earliest models developed for modeling the pressure drop for the flow across a porous medium. Darcy found that the area-averaged fluid velocity passing through a porous media was directly proportional to the pressure gradient and inversely proportional to the fluid dynamic viscosity (μ) (Bejan, Dincer, Lorente, Miguel, & Reis, 2004). The constant of proportionality was found to be the permeability of the medium, and has the units of m^2. Darcy's law is, however, only valid for viscously dominated flows, as it only includes viscous resistance. The law was modified and more generalized models were developed to allow it to be valid for inertially dominated flows. Forchheimer (Lage, 1998) added an inertial loss term in addition to the viscous loss term by Darcy. Joseph, Nield, and Papanicolaou (1982) added to Forchheimer's modified model a factor to account for the inertial resistance. Other than using Darcy-Forchheimer formula, a drag force term can be added to the momentum equation, to account for the momentum loss resulting from the porous medium. Studies summarized in Table 1 have utilized different formulations of the porous media model to study different configurations.

1.3. Motivation and objectives

In previous literature, a number of direct relations between the porosity ratio and the pressure loss were provided (Lee & Lim, 2001; Perry & Green, 2008; Reynolds, 1969). Examples for previous studies that derived empirical for the pressure drop across porous windbreaks are provided in Table 2.

Currently, the experimental data are the sole reliable method to obtain the coefficients for the porous media model. None of the previous literature derived correlations between the porosity ratio of a perforated surface and the resistance coefficients of the porous media model. The novelty of this research is that it directly provides the needed coefficients for running the porous media model for a range of porosity ratios ($\phi = 0.25$–0.6) without resorting to extensive experimental work.

This paper is structured as follows: the details for the experimental

Table 2
Derived relations for the pressure loss across a porous medium.

Authors and year	Porosity ratio	Method	Relation for ΔP
Minoru, Shintarou, Koumei, and Fumiaki (2014)	0.35–0.88	Experimental	Inversely proportional to porosity
Özahi (2015)	0.064–0.331	Experimental	Exponential with porosity
Arya, Novak, Saito, Levy, and Sottile (2019)	0.064–0.331	Experimental	Power law with velocity
Gan and Riffat (1997)	0.5	Numerical	Inversely proportional to t/d

Table 3
Perforated surfaces holes dimensions and corresponding porosity.

Hole diameter d (mm)	Porosity (ϕ)
2.95	0.25
3.2	0.3
3.45	0.35
3.7	0.4
4.15	0.5
4.55	0.6

setup and the numerical simulations are explained in Section 2. Hence, the results obtained from the experiments and the CFD simulations are presented and discussed in Section 3. Finally, Section 4 provides concluding remarks and recommendations for future work.

2. Methods

In this section, the methods used for conducting experiments and performing numerical CFD simulations are explained. The first two subsections provide the details for the PIV and pressure measurements respectively. The last subsection discusses the details for numerical simulations.

2.1. Perforated surfaces geometry

Fig. 2 shows the typical geometry of the thermally 3D printed perforated surface considered in this study. For each surface, the width (b) is 60 cm, height (h) is 7.5 cm and the thickness (t) is 3 mm. Thus, the aspect ratio for the perforated surface, defined by the ratio of the surface width to its height, is $b/h = 8$. The surface is perforated by using circular shaped holes that are uniformly distributed. The distance between the holes' centers (l) is 10 mm in the vertical direction and 7 mm horizontally. The porosity ratio for each perforated surface is defined as the ratio between the empty area (total area of the circular holes) and the total area. For each surface, the porosity is changed by changing the diameter (d) of the holes. For all models the total number of holes is fixed to 1666 holes. Fig. 2 also indicates the locations where velocity measurements were examined, namely $y/h = 0.8$ and $y/h = 1.2$. Table 3 shows the values for the different hole diameters and the corresponding porosity value.

2.2. PIV experiment setup

All experiments were performed at Qatar University wind tunnel of a test section of $2 \times 2\,\mathrm{m}^2$. The Reynolds number considered in this study is $Re = 10^5$, and the reference length is the height of the perforated surface $h = 7.5\,\mathrm{cm}$. The Reynolds number for the perforated surfaces holes ranged between $Re \approx 400$ to $Re \approx 625$. When the perforated surface scaled model is fixed inside the wind tunnel, it resulted in a blockage ratio of 1.1% of the testing section area.

For PIV measurements, the scaled models were positioned in the wind tunnel test section such that it allows the cameras to record images
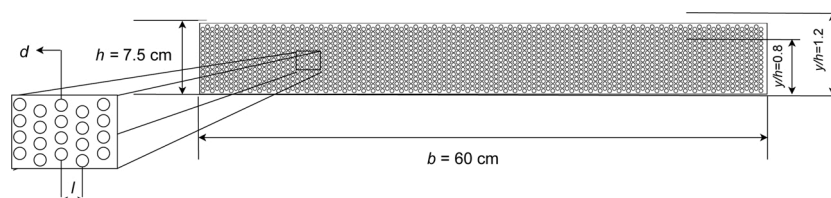
clear from any obstacles and avoid laser reflections. The laser used is Litron dual pulse Nd:Yag laser with a wave length of 550 nm and 1000 mW power. The camera is FlowSense EO 4M with 2048×2048 pixels resolution and a frame rate of 20 frames per second (FPS). The schematic in Fig. 3 shows the PIV experiment setup and its devices. For post-processing of the results of the PIV experiment, DynamicStudio software was used (DynamicStudio User's Guide (Dantec Dynamics, 2012)). For each perforated surface, a total of 50 instantaneous velocity fields were obtained, and the average was evaluated. The time between the laser pulses was 600 μs. For cross-correlation, a two-step algorithm is used with an interrogation area of 32×32 pixels, with 50% horizontal and vertical overlap.

2.3. Pressure drop measurement

The pressure drop is evaluated using the pressure coefficient (C_p), which is defined as:

$$C_p = \frac{p - p_0}{0.5\rho U_0^{\,2}}, \tag{1}$$

where (p) is the pressure at the point, (p_0) is the reference pressure, (ρ) is air density and (U_0) is the reference free stream velocity.

The pressure difference is measured by pressure taps positioned at the wind tunnel's ground level upstream and downstream the model. The reference pressure p_0 is taken at a distance 4.667 times the height of the surface, such that the pressure is not affected by the presence of the model. The origin ($x/h = 0$) is where the perforated surface model is located. A total of 14 pressure taps were placed at ground level, such that there are seven taps upstream and downstream the model. The pressure taps covered the distance starting from $x/h = -3.33$ upstream and ending at $x/h = 3.33$ downstream the model. Table 4 reports the pressure taps locations in either sides of the model. The pressure transducer Setra MR1SP is used with an accuracy of $\pm 1\%$. Fig. 4 shows a schematic for the setup used in the experiment for pressure measurement, and the locations of the pressure taps corresponding to Table 4. The pressure values were measured at ground level because it provides more accurate results than introducing pressure measurement probes into the air flow. Whereas for the velocity, it is more convenient to measure it at a certain height because at the walls, the no slip boundary condition affects the values. Moreover, non-intrusive PIV provides velocity measurement without affecting the flow-field.
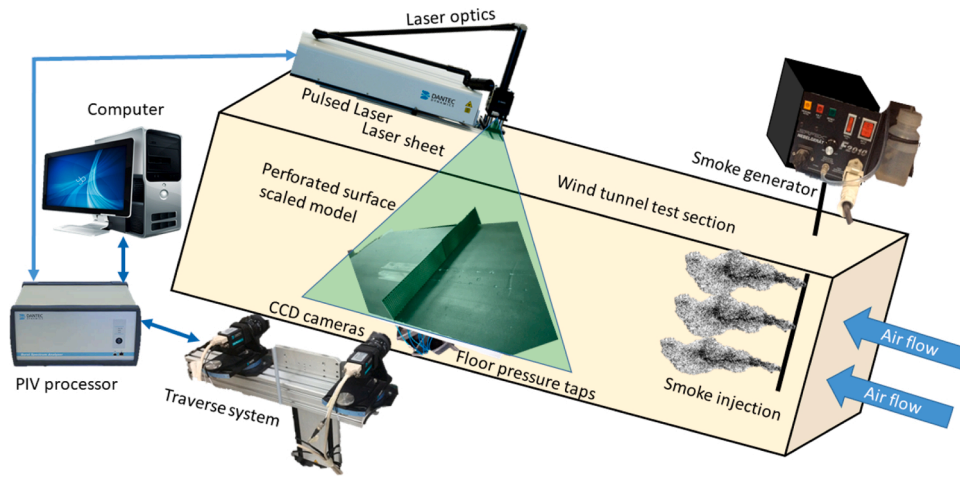

Fig. 2. Perforated surface geometry and dimensions definition.

Fig. 3. Setup for the PIV experiment.

Table 4
Pressure taps locations upstream and downstream the model.

Tap no.	1	2	3	4	5	6	7
Distance from surface (x/h)	±0.13	±0.53	±1	±1.33	±2	±2.67	±3.33

2.4. Numerical simulations

2.4.1. Mathematical model

In this study, the reference free stream velocity is low and the incompressible continuity and momentum equations are used to simulate the airflow. The governing equations for the steady flow are as follows:

$$\nabla \cdot \boldsymbol{u} = 0,$$

$$(\boldsymbol{u} \cdot \nabla)\boldsymbol{u} = \nu \nabla^2 \boldsymbol{u} - \frac{1}{\rho}\nabla p - \boldsymbol{S}_{\text{porous}}, \tag{2}$$

where $\boldsymbol{u} = [u, v, w]^T$ is the velocity vector, p is the pressure, ν is the kinematic viscosity and ρ is the air density. $\boldsymbol{S}_{porous}$ is the source term due to the presence of the porous media, and is only considered when using the porous media model.

ANSYS Fluent uses the generalized formula to model porous media, as detailed in Fluent user manual (ANSYS Fluent User Guide, Release 15.0). The porous media model in ANSYS uses a superficial velocity inside the porous media instead of the actual velocity in the media. Thus,

the model cannot predict the real velocity inside the media. However, it produces results for the pressure drop and velocity values. The modeling for the porous media uses the sink term $\boldsymbol{S}_{porous}$, which is defined as follows ANSYS Inc (2013):

$$\boldsymbol{S}_{\text{porous}} = \nu \mathbf{D}\boldsymbol{u} + \frac{1}{2}|\boldsymbol{u}|\mathbf{C}\boldsymbol{u}, \tag{3}$$

where $\mathbf{D}$ is the matrix of viscous resistance coefficients, which is a diagonal matrix containing the resistance coefficient corresponding to each direction. $\mathbf{C}$ is the matrix of inertial resistance coefficients, which has a diagonal form similar to the matrix $\mathbf{D}$. The terms appearing in Eq. (3) are called Darcy and Forchheimer drag terms (Joseph et al., 1982). If any of the matrices had equal diagonal elements, this means that it is assumed that the modeled porous media is isotropic. However, this is not the case for the perforated surface, as the resistance in the direction normal to the surface plane is less than its counterparts in the other two directions. The diagonal elements of matrix $\mathbf{D}$ are the viscous resistance coefficients, which are the inverse of the porous media permeability α that corresponds to each direction. While the diagonal elements of matrix $\mathbf{C}$ are the inertial resistance coefficients C_2 that correspond to the x, y and z directions respectively. The effect of using surfaces of different porosity values is considered by varying the coefficients of matrices $\mathbf{D}$ and $\mathbf{C}$.

The turbulence is modeled using the k-ε Reynolds averaged Navier–Stokes (RANS) model with enhanced wall treatment. Reynolds averaging of Eq. (2) results in source terms due to the porous media model appearing also in the k and ε equations of the turbulence model.
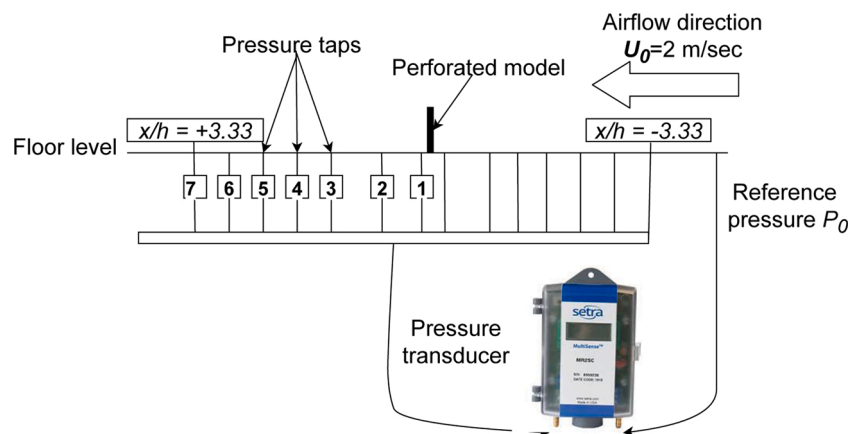

Fig. 4. Schematic for the pressure measurement experiment setup and the pressure taps' locations.

The equations for the $k - \varepsilon$ RANS turbulence model are as follows:

$$\boldsymbol{u} \cdot \nabla k = \nabla \cdot \left(\frac{\nu_t}{\sigma_k} \nabla k \right) + P_{\text{tke}} - \varepsilon + S_k,$$

$$\boldsymbol{u} \cdot \nabla \varepsilon = \nabla \cdot \left(\frac{\nu_t}{\sigma_k} \nabla \varepsilon \right) + C_{\varepsilon 1} \frac{\varepsilon}{k} P_{\text{tke}} - C_{\varepsilon 2} \frac{\varepsilon^2}{k} + S_{\varepsilon}, \quad (4)$$

where is k is the turbulent kinetic energy, ε is the dissipation rate, ν_t is the turbulent viscosity, σ_k is the von Karman constant, $C_{\varepsilon 1}$ and $C_{\varepsilon 2}$ are the $k - \varepsilon$ model constants, and S_k and S_{ε} are the source terms defined by the porous media model. The production of the turbulent kinetic energy P_{tke} is defined as:

$$P_{\text{tke}} = \nu_t \left(\nabla \boldsymbol{u} + (\nabla \boldsymbol{u})^T \right) \otimes \nabla \boldsymbol{u}, \quad (5)$$

where $\nabla \boldsymbol{u}$ is the gradient of the mean velocity field and the symbol $\otimes$ is a tensor contraction symbol.

2.4.2. Computational domain and boundary conditions

The computational domain used for simulations for the solid wall and for the exact geometry cases is of the same size. It is sufficiently large so the boundaries are not affected by the flow adjacent to the perforated model geometry. The domain is ten times the perforated model height upstream, above and to its sides, while it has a length of 20 times the perforated model height downstream. Symmetry boundary condition was used at the middle of the surface to reduce computational cost. Fig. 5 shows the details of the computational domain and the different computational boundaries. In Table 5, the size and quality parameters associated with the grids of the exact geometry and the approximated solid wall models are reported. Table 6 shows the boundary conditions assigned to each surface boundary illustrated in Fig. 5.

Second-order upwind schemes are used for discretizing the momentum, k and ε equations. Gradient evaluation is performed using

Table 5
Grid size and quality parameters.

		Exact geometry	Solid geometry
Mesh size	Number of cells	23377798	2908750
	Number of nodes	4439711	559154
Quality	Maximum aspect ratio	25.57	20.25
	Maximum skewness	0.9	0.87
	Minimum orthogonal quality	2.21e−2	3.46e−2

Table 6
Boundary conditions for each surface group.

Surface group	Boundary condition type	Value
Inlet	Velocity inlet	$U_0 = 2 \, \text{m/s}$
Outlet	Pressure outlet	Zero gauge pressure
Leeward and windward sides (exact geometry)	No-slip wall	Roughness height = 0 m
Leeward and windward sides (porous media model)	Interior surfaces	N/A
Upper wall and sides of perforated surface	No-slip wall	Roughness height = 0 m
Ground	No-slip wall	Roughness height = 0 m
Symmetry	Symmetry	–

least-squares. The simulation was kept running until the residuals for all equations were reduced to values below 10^{-4}. Different mesh sizes were examined ranging from number of cells of one million and up to 17 million grid cells. Fig. 6 summarizes the results of the grid sensitivity study for both the exact geometry and the solid cases using the porous media model. The grid sensitivity study was performed by examining the variation of the pressure drop across the windbreak model, rather than
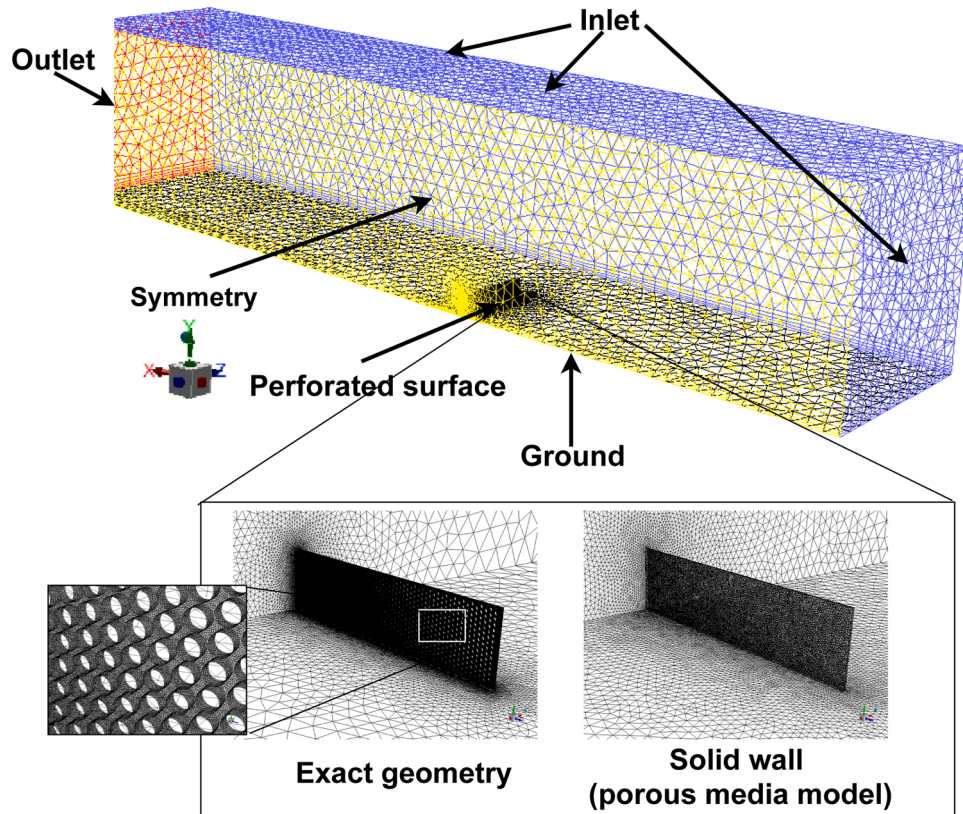

Fig. 5. Computational domain used in CFD simulations and grid generated for the exact geometry and the solid wall model. Magnified view shows the grid generated for the perforation holes of the exact geometry.
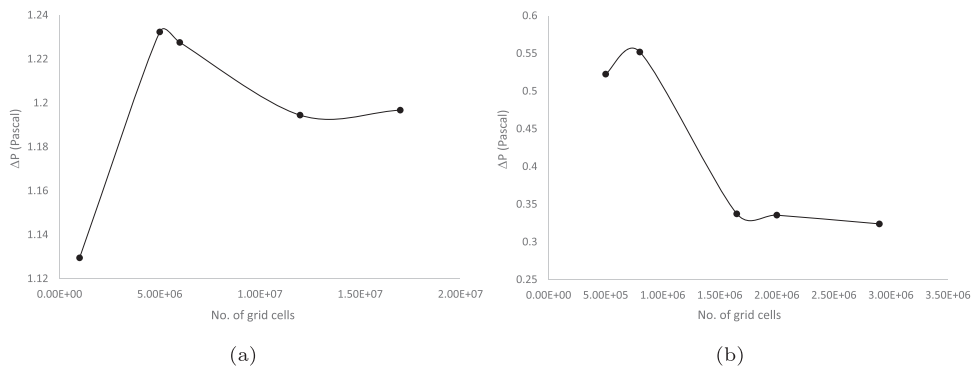
Fig. 6. Grid sensitivity study for the numerical simulations of the (a) exact geometry and (b) the solid geometry using the porous media model.

the whole computational domain. Panel (a) of Fig. 6 shows that for a grid size of 17 million cells, the value of the pressure drop value does not vary with further mesh refinement for the exact geometry. Hence it was decided to use a grid of 17 million cells. Panel (b) shows that a grid of two million cells is sufficient to simulate the airflow using the porous media model as the pressure drop value does not vary with further mesh refinement. The perforated model solid geometry is defined as a separate fluid domain. The effect of the perforation is included by applying the porous media model formulation when solving for the flow variables inside this domain. The computational cost saving is clear, as the difference between the grid sizes is almost one order of magnitude.

3. Results and discussion

The results for the parametric study are discussed in this section and used to develop formulae for the porous media model coefficients. At the end of the section, the results of the porous media model are validated against experimental data to assess the accuracy of the derived correlation equations.

3.1. Experimental results

Fig. 7 shows the velocity vectors superimposed over the contours of velocity magnitude for the perforated surfaces as obtained from the PIV measurements. In panel (a), the porosity ratio is $\phi = 0.3$ and in panel (b) it is $\phi = 0.5$. The free stream wind velocity is $U_0 = 2\,\text{m/s}$. The vectors shown are averaged from 50 instantaneous velocity fields. By comparing panels (a) and (b) of Fig. 7, it is evident that the effect of increasing the porosity ratio is the increase in the velocity magnitude downstream the perforated surface model. Above the models, the flow accelerates, but this accelerations is also dependent on the porosity ratio. As the porosity

ratio increases, the perforated model presents less resistance to the airflow. Thus, the flow downstream is becoming more uniform. Due to the experimental limitations of PIV measurements near solid surfaces, the vectors near the wall and close to the porous fence model have irregular pattern. Inherently, solid surfaces can trap the seeding particles, which reduces the seeding uniformity, thus, introducing an experimental error. Moreover, the shadow of the porous fence model can be seen and is affecting the velocity readings right upstream the model.

Figs. 8 and 9 show the variation of the pressure coefficient (C_p) and velocity magnitude (U/U_0) with porosity ratio for the perforated surfaces. Results shown in the figures are from experimental pressure measurement and PIV runs. The pressure is measured at ground level, while the velocity is measured at a height of $y/h = 1.2$ above the ground
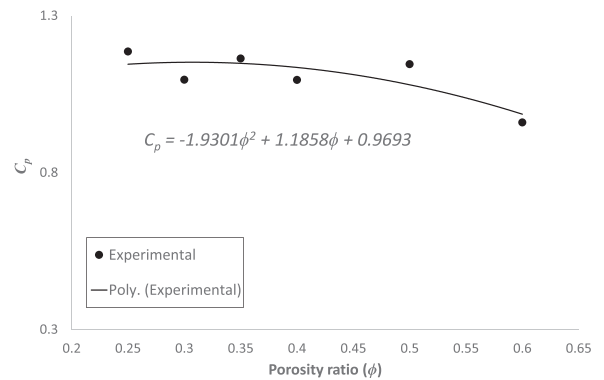

$$C_p = -1.9301\phi^2 + 1.1858\phi + 0.9693$$

Fig. 8. Experimental results for the pressure coefficient (C_p) variation against porosity ratio (ϕ).

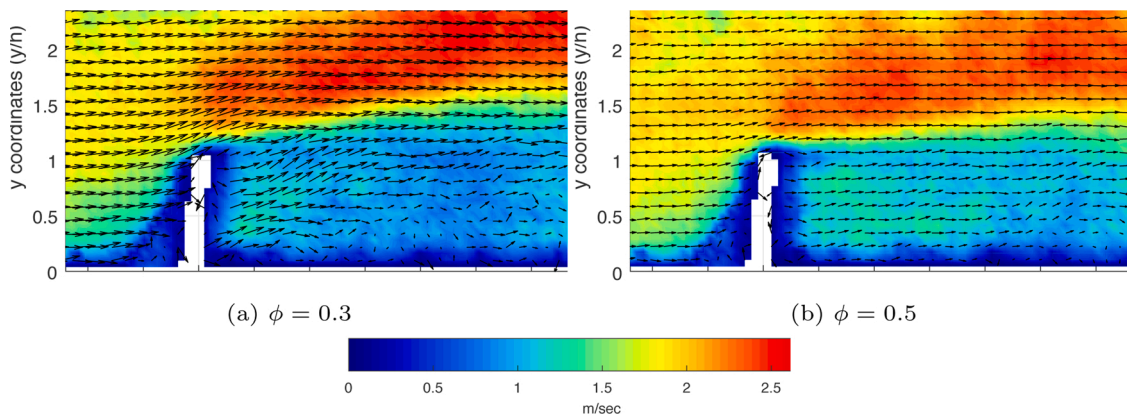(a) $\phi = 0.3$

(b) $\phi = 0.5$

Fig. 7. Velocity vectors obtained from PIV experiments superimposed over contours of velocity magnitude for perforated surfaces with porosity of (a) $\phi = 0.3$ and (b) $\phi = 0.5$.
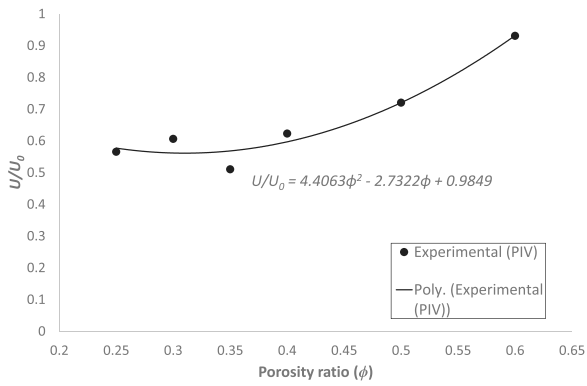
Fig. 9. Experimental PIV results for velocity magnitude (U/U_0) variation against porosity ratio (ϕ).

level. This height was selected because it is the height with the least uncertainty in terms of experimental PIV results. At lower heights, the particles accumulating at the windward side of the fence do not go through the fence, and this lead to a decrease in seeding density, which in turns increases the error. Even though this height is above the fence, the effect of varying the porosity ratio is captured (Heisler & Dewalle, 1988).

The results in Figs. 8 and 9 are used to obtain regression equations linking the velocity magnitude and the pressure coefficient to the model's porosity ratio. Six models are used to obtain the regression models, each one corresponding to a single porosity value, which provides a sufficient number of data points to obtain relations between the porosity ratio and the pressure drop based on the methodology followed by Minoru et al. (2014) and Özahi (2015). To fit the experimental data, a second order regression model was used for both the pressure coefficient and the velocity magnitude variation with porosity ratio. The quadratic relation for the the pressure drop with the porosity ratio is:

$$C_p = -1.9301\phi^2 + 1.1858\phi + 0.9693. \tag{6}$$

Whereas for the velocity, the relation is as follows:

$$U/U_0 = 4.406\phi^2 - 2.732\phi + 0.985. \tag{7}$$

The regression models shown in figures are only valid for the range of porosity ratios covered in this study.

3.2. Porous media model parametric study

In this subsection, the results of the pressure and velocity variations across the perforated surfaces are presented. The CFD results are for the exact geometry and for the simulations using the porous media model. The purpose of comparisons is to establish a relationship between the porous media model and the exact geometry case.

A parametric analysis study was carried out to establish the effect of the inertial and viscous resistance coefficients on the pressure and velocity across the perforated surfaces. The velocity magnitude monitored was at a height of $y/h = 1.2$, and at a distance of $x/h = 1.067$ downstream the model, while the pressure coefficient was monitored at ground level downstream the model. The positions for monitoring the velocity and pressure values were selected to match the PIV grid and the experimental pressure reading location. Fig. 10 shows the variation of the velocity magnitude and the pressure coefficient with different viscous and inertial resistance coefficients of the porous media model. The viscous resistance coefficient in the x-direction ($1/\alpha_x$) covered values ranging from 6×10^6 m^{-2} to 5.9×10^7 m^{-2}, while the x-direction inertial resistance coefficient ($C_{2,x}$) values covered the range from 100 m^{-1} to 2000 m^{-1}. The selection of the ranges for the inertial and viscous resistance coefficients was based on a sensitivity study involving iterative numerical simulations while randomly varying the porous model coefficients. The ranges were selected based on the values that can produce velocity and pressure values close to their experimental counterparts. With regard to the velocity, the drop appears to be quadratic with increasing the inertial or viscous resistance. However, the drop in pressure coefficient is quadratic when varying the inertial resistance coefficient, and linear when varying the viscous resistance coefficient. This behavior is attributed to the form of the porous media model (Eq. (3)).

Based on the results of the parametric study, six porous models with different viscous and inertial resistance coefficients values are selected

Table 7
Coefficients used for porous media model simulations.

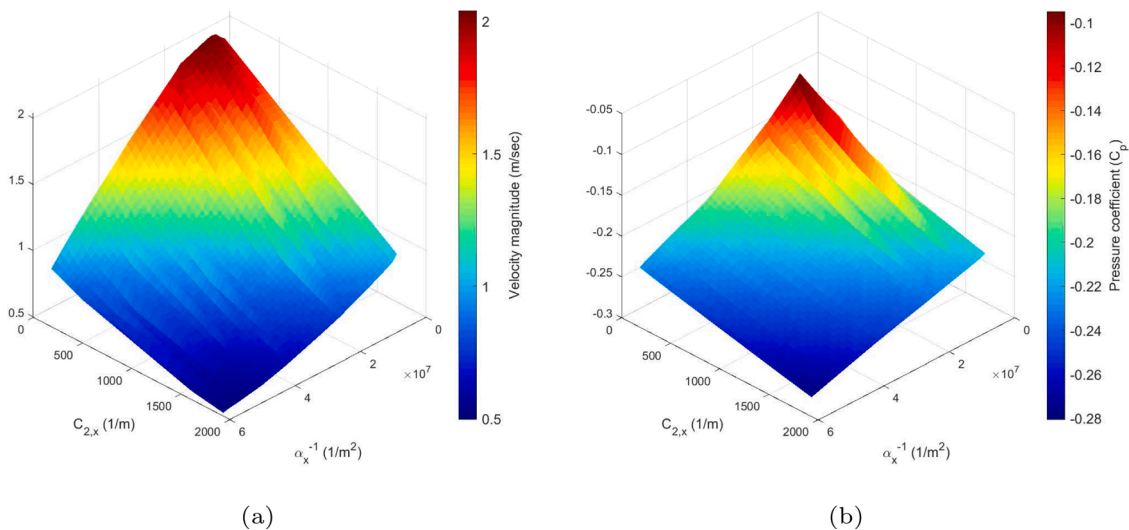| Model no.	Viscous resistance $1/\alpha_x$ (m^{-2})	Inertial resistance $C_{2,x}$ (m^{-1})
1	25×10^6	650
2	22.5×10^6	575
3	20×10^6	500
4	17×10^6	450
5	14×10^6	375
6	12×10^6	300

(a)

(b)

Fig. 10. Variation of (a) velocity and (b) pressure coefficient C_p as a function of the x-component of the inertial and viscous resistance coefficients.

for further analysis, as depicted in Table 7. Figs. 11 and 12 compare the variation of the velocity magnitude in the streamwise direction U/U_0 (normalized by the free stream velocity) of the porous models against PIV velocity results. The velocity is obtained at heights of $y/h = 1.2$ and $y/h = 0.8$. Whereas Fig. 13 shows the variation of the pressure coefficient at ground level upstream and downstream the perforated surface.

As depicted in Figs. 11 to 13, the porous media model was able to capture the general behavior of the velocity and pressure drop variation across the perforated surface. However, the comparison with PIV velocity results showed better agreement than the pressure drop.

With regard to the velocity variation, Fig. 11, a direct correspondence between the porous media models and the exact perforated model geometry cannot be made for all models. However, and a correspondence between models 2, 3, 4 and 6 (Table 7) and the surfaces with porosity ratios of $\phi = 0.3$, 0.4, 0.5 and 0.6, respectively, can be established and they can be compared to each other. The velocity value downstream model 1 are out of range and are less than the model with porosity ratio $\phi = 0.25$. Whereas for model 5, the downstream velocity values are in-between the ones corresponding to the models with porosity ratios $\phi = 0.5$ and $\phi = 0.6$. Therefore, models 1 and 5 were eliminated from the comparison. The peak velocity was captured for porosity ratios of $\phi = 0.4$, 0.5 and 0.6, with underestimation of the peak velocity for other porosity ratios. For all porosity ratios, the velocity decrease downstream, up to downstream distance of $x/h = 3$, was well-captured by the porous media model. Table 8 provides numeric values for the computed root mean squared error for the comparison of velocity magnitude at different streamwise segments. From Table 8, the results show better agreement in the upstream segment, with a maximum average error of 4.5% when comparing model 4 and $\phi = 0.5$. The results downstream have less agreement with a maximum average absolute error of 11.8% when comparing model 3 and $\phi = 0.4$. The numeric values for the peak velocity errors are intermediate between the ones yielded for the velocity upstream and downstream. The general behavior is that further downstream, the agreement with experiments becomes less. The reason for the discrepancy is that in the porous media model, the viscous effects due to the small holes were not completely captured. The results of velocity magnitude at $y/h = 0.8$ show good agreement with the experiment only downstream the porous fence model. It should be added that, there is an inherent error in the PIV measurements resulting from the seeding uniformity being affected by particles impacting the fence.

With regard to the results for the pressure in Fig. 13, the behavior upstream the perforated surface is well captured. However, the pressure downstream the surface is underestimated except for porosity ratio of $\phi = 0.6$.
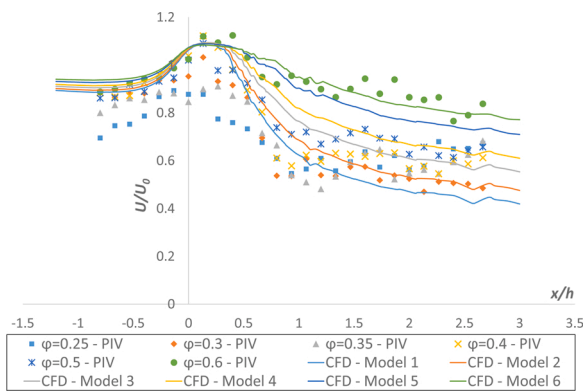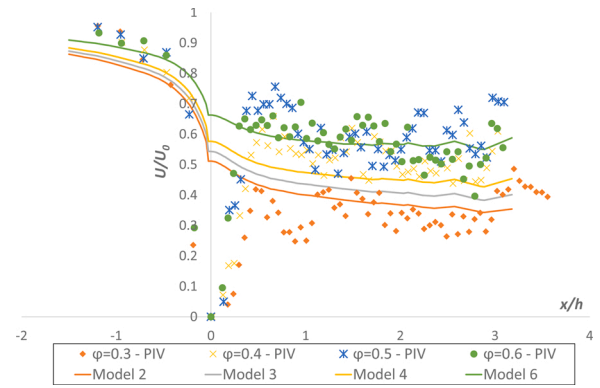

Fig. 12. Streamwise velocity magnitude variation (U/U_0) across the perforated surface at a height of $y/h = 0.8$ obtained from PIV results and CFD simulations using the porous media model.
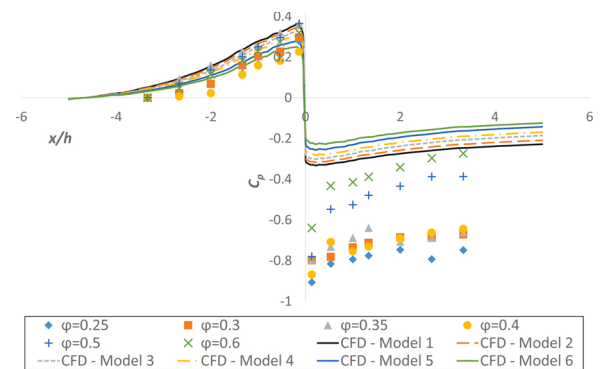

Fig. 13. Streamwise variation of the pressure coefficient (C_p) at ground level for the perforated surface obtained from pressure measurements and CFD simulations using the porous media model.

Table 8
Average error in velocity magnitude (U/U_0) from comparison of results of CFD using porous media model to experimental PIV results at different segments.

Comparison between	Upstream ($x/h = -0.8$ to -0.1)	Peak ($x/h = -0.1$ to 0.5)	Downstream ($x/h = 0.5$ to 2.5)
Model 2 and $\phi = 0.3$	3.2%	10.6%	10.9%
Model 3 and $\phi = 0.4$	2.3%	3.9%	11.8%
Model 4 and $\phi = 0.5$	4.5%	6.7%	7.7%
Model 6 and $\phi = 0.6$	3.4%	2.9%	4.7%

3.3. Numerical simulation results

In this subsection, the results from the CFD simulations for the exact geometry and the porous media model are presented and discussed. The results shown for the exact geometry are for the model with porosity ratio of $\phi = 0.5$. Whereas the results shown for the solid geometry are for the porous media model 4 from Table 7. The model has a viscous resistance coefficient in the x-direction of $1/\alpha_x = 1.7 \times 10^7 \, \text{m}^{-2}$ and inertial resistance coefficient in the x-direction of $C_{2,x} = 450 \, \text{m}^{-1}$. The values for the empirical coefficients were selected to simulate a similar perforated model with a porosity ratio of 0.5. These values were selected based upon the results of the sensitivity analysis that were shown in Section 3.2. The velocity values obtained in the parametric study (Fig. 10) were compared to their experimental counterparts evaluated at the same location, and the corresponding porous media parameters

Fig. 11. Streamwise velocity magnitude variation (U/U_0) across the perforated surface at a height of $y/h = 1.2$ obtained from PIV results and CFD simulations using the porous media model.

values are used. To define a porous media model we also need the resistances in the other two-directions are also needed. The values for the viscous and inertial resistance coefficients in y and z directions are selected to be sufficiently large to represent solid geometry and only allow flow in the x-direction within the porous element. For the y and z directions, the viscous and inertial resistances are set to $1/\alpha = 2 \times 10^9$ and $C_2 = 2.2 \times 10^5$, respectively. These values for the inertial and viscous resistance coefficients in the y and z directions are fixed all numerical simulations performed using the porous media model.

Figs. 14 and 15 show the contours of the pressure coefficient C_p at the symmetry plane. Panel (a) shows the results obtained by simulating a solid wall and using the porous media model, while panel (b) shows the results obtained for the exact geometry. Both panels of Fig. 14 show similar pressure contours. However, for the case of the exact geometry (panel (b)), the effect of the small holes can be seen downstream the fence. In both panels of Fig. 14, the pressure rises just right upstream the perforated surface, and immediately drops after. The minimum pressure coefficient value is captured right after the perforated model, while the maximum pressure coefficient value is captured just right upstream. In panels (a) and (b) of Fig. 15, the effect of the presence of the model walls is shown by the pressure coefficient variation at ground level. In panel (b) of Fig. 15, the details of the pressure drop across the small holes in the exact geometry can be seen. Additional differences are the maximum and minimum pressure coefficient values, which are due to the physical presence of the holes in the exact geometry, which are not considered in the solid wall case.

Fig. 16 show the contours of the velocity magnitude at the symmetry plane. Panel (a) shows the results obtained by simulating a solid wall and using the porous media model, while panel (b) shows the results obtained for the exact geometry. In both panels of Fig. 16, a similar pattern for the velocity field can be identified. The velocity rises due to acceleration and then decreases after passing through the perforated model. The only detail that can be seen in panel (b) of Fig. 16 and not captured in panel (a), is the wake due to the flow passing through the small holes of the model.

3.4. Formulation and validation of empirical formulae

From the parametric analysis performed and the porous media models tested (Section 3.2), a relation between the velocity to the inertial resistance coefficient in the x-direction $C_{2,x}$ can be obtained. The velocity at a distance $x = 1.067h$ downstream the model and at a height $y = 1.2h$ was monitored for the porous media models examined, as per Table 7. The location where the value of the velocity magnitude was monitored is selected in order to be able to directly compare the results to their counterparts obtained from PIV runs. Fig. 17 shows the variation of the velocity downstream with the inertial resistance coefficient. Based

on the regression line displayed in the figure, the relation between the inertial resistance coefficient and the velocity magnitude is linear. For practical applications, it is useful to obtain an equation able to estimate the inertial resistance coefficient $C_{2,x}$ as a function of porosity ratio ϕ. Using the correlations from Figs. 9 and 17, an empirical equation relating the inertial resistance coefficient ($C_{2,x}$) to the porosity ratio (ϕ) can be obtained. Fig. 18 summarizes the results obtained for the relation between the inertial resistance coefficient and the porosity ratio. Based on the previous analysis, a linear equation relating the porosity ratio of a perforated surface to the inertial resistance $C_{2,x}$ was obtained, as follows:

$$C_{2,x} = -1452.2\phi + 1214.6. \tag{8}$$

Similar to the inertial resistance formula methodology, a relation between the velocity and the viscous resistance coefficient in the x-direction ($1/\alpha_x$) can be obtained. The velocity located at a distance $x = 1.067h$ from the perforated surface was measured while varying the viscous resistance coefficient $1/\alpha_x$ for the porous media model. Fig. 19 shows the variation of the velocity downstream with the viscous resistance coefficient. The velocity monitored is at a height of $y/h = 1.2$ and at a distance $x/h = 1.067$ downstream the model. Based on the regression line displayed in the figure, the relation between the velocity magnitude varies linearly with the viscous resistance coefficient. From Figs. 9 and 19, a relation between the inertial resistance coefficient ($1/\alpha_x$) and the porosity ratio (ϕ) can be obtained. The empirical formula, relating the viscous resistance coefficient $1/\alpha_x$ and the porosity ratio ϕ, have important practical applications. Fig. 20 summarizes the results obtained for the relation between the inertial resistance coefficient and the porosity ratio. A polynomial equation relating the porosity ratio of a perforated surface to the viscous resistance $1/\alpha_x$ was obtained, as follows:

$$1/\alpha_x = (-9\phi^2 + 2\phi + 3) \times 10^7. \tag{9}$$

In order to validate the obtained empirical formulae (Eqs. (8) and (9)), the porous media model results are compared to experimental results and the CFD of the exact geometry. The comparison is shown in panels (a) to (c) of Fig. 21 and is for porosity ratio $\phi = 0.5$. The velocity was measured at heights $y/h = 1.2$ and $y/h = 0.8$ (panels (a) and (b) respectively), while the pressure was measured at the ground level (panel (c)).

Table 9 summarizes the results of comparing the porous media model results with their counterparts from experiments and the CFD of the exact geometry. The values in Table 9 are the root mean square errors obtained from comparing the results in Fig. 21. The velocity comparison showed good agreement with both experimental and exact geometry CFD results. However, for the pressure drop, less agreement with experimental results was attained. On the other hand, the pressure drop by using the porous media model showed good agreement with the CFD
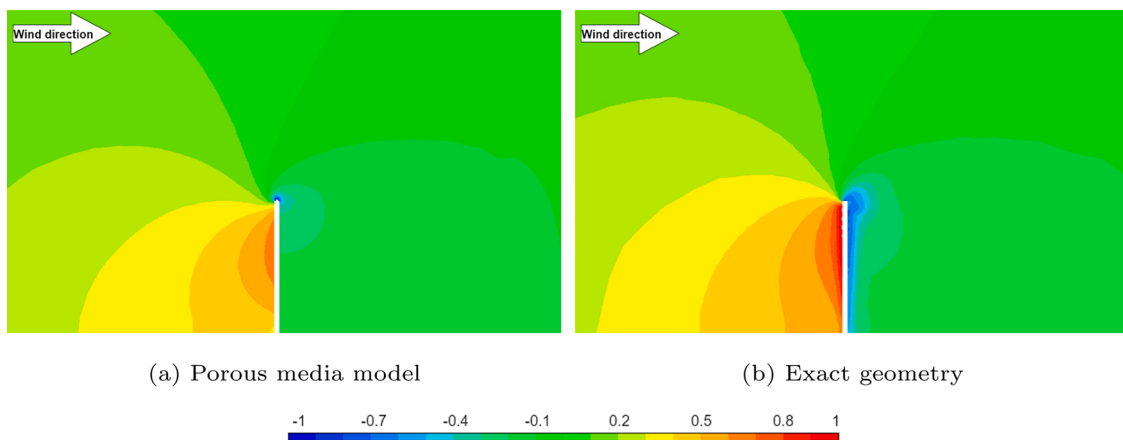
(a) Porous media model   (b) Exact geometry

-1   -0.7   -0.4   -0.1   0.2   0.5   0.8   1

Fig. 14. Contours of pressure coefficient C_p at the symmetry plane for (a) the porous media model and (b) the exact geometry – Porosity ratio $\phi = 0.5$.
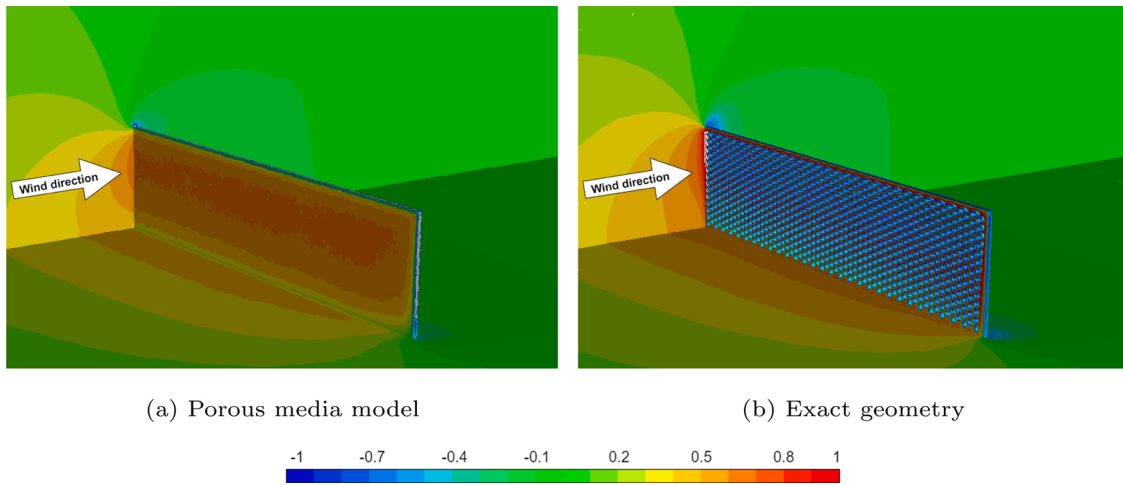
(a) Porous media model

(b) Exact geometry

Fig. 15. Isometric view for the contours of pressure coefficient C_p for (a) the porous media model and (b) the exact geometry – Porosity ratio $\phi = 0.5$.
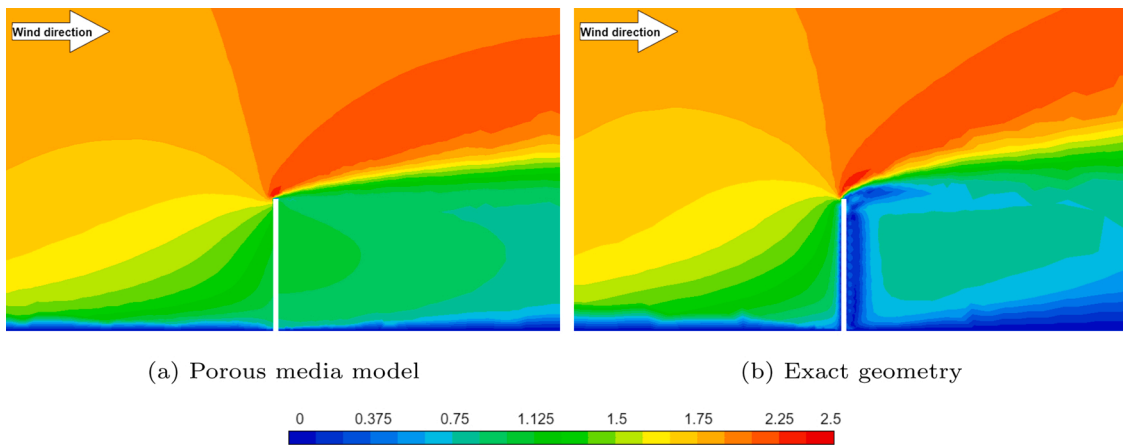

(a) Porous media model

(b) Exact geometry

Fig. 16. Contours of velocity magnitude at the symmetry plane for (a) the porous media model and (b) the exact geometry – Porosity ratio $\phi = 0.5$.
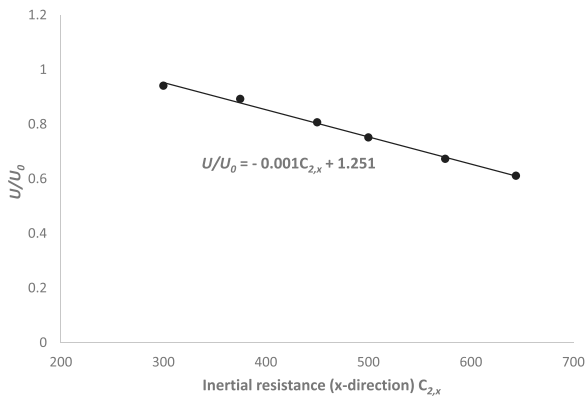

Fig. 17. Velocity magnitude (U/U_0) variation against the x-direction inertial resistance of porous media ($C_{2,x}$) obtained from CFD simulations.
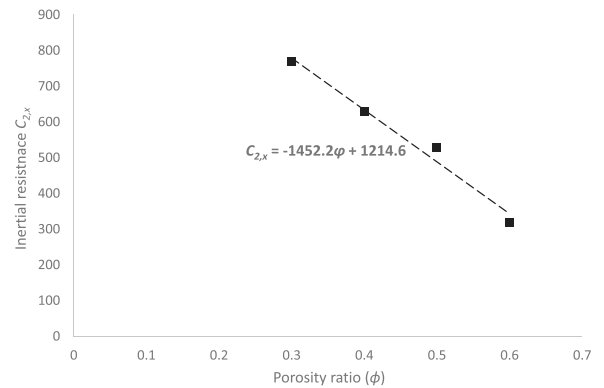
Fig. 18. Variation of the x-direction inertial resistance coefficient ($C_{2,x}$) against porosity ratio (ϕ).

simulation of the exact geometry. In comparison to the experimental results, the porous media model yielded an average error of 6.4% and 21.7% in the velocity values at heights of $y/h = 1.2$ and $y/h = 0.8$, respectively, and of about 26% in the pressure drop. This discrepancy is attributed to the fact that near the real model, viscous effects dominate which are not fully captured by the porous media model. Looking at panels of Fig. 21, one can see that in the region from $x/h = -0.1$ to $x/h = 0.3$, the porous media model performs worst compared to other

locations. The comparison of the velocity values of the porous media model to their counterparts from the CFD of the exact geometry yielded an average error of 8%. The comparison with the results of CFD of the exact geometry showed better agreement in terms of pressure, with an average error of 12%. The comparison with the pressure coefficient obtained from CFD of the exact geometry show similar behavior to the results obtained by Nowak (2016). The pressure drop spike downstream the perforated surface captured by the CFD simulation for the exact
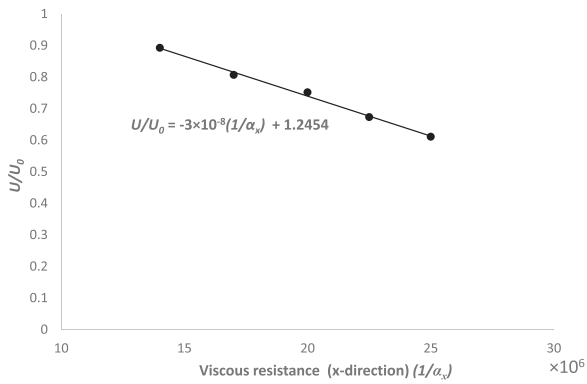
Fig. 19. Velocity magnitude (U/U_0) variation against the x-direction viscous resistance of porous media ($1/\alpha_x$) obtained from CFD simulations.
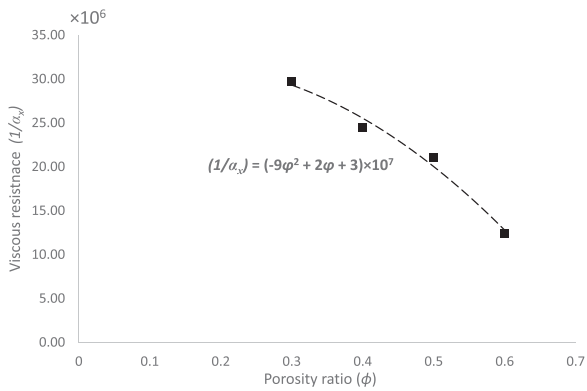

Fig. 20. Viscous resistance coefficient ($1/\alpha_x$) variation against porosity ratio (ϕ) of perforated surface.

geometry is predicted by the porous media model, and the pressure drop across the surface is linear. For all cases, the CFD pressure results are in less agreement than velocity results. This pattern is attributed to the viscous losses associated with the physical presence of the small circular holes in the exact geometry of the perforated model. The pressure upstream the porous model had better agreement, and the majority of the results deviation comes from the disagreement in the wake downstream the model.

Table 9 compares the results from porous media model with their counterparts from experiments and the exact geometry CFD simulation using statistical model performance measures as presented by Chang and Hanna (2004). The measures used were: the fractional bias (FB), geometric mean bias (MG), the geometric variance (VG), and the correlation coefficient (R). A perfect match model will yield a fractional bias of zero, and a value of one for MG, VG and R. Compared to the CFD simulation of the exact fence geometry, the statistical performance indicators show that the porous media model yielded the best performance for FB, MG and VG values. However, for the velocity at $y/h = 0.8$, the correlation coefficient (R) was about 0.78, as the porous media model does not capture the viscous effects. Nevertheless, the velocity and pressure profiles are not captured near the solid wall representing the porous windbreak, their values are captured accurately upstream and downstream of the windbreak.
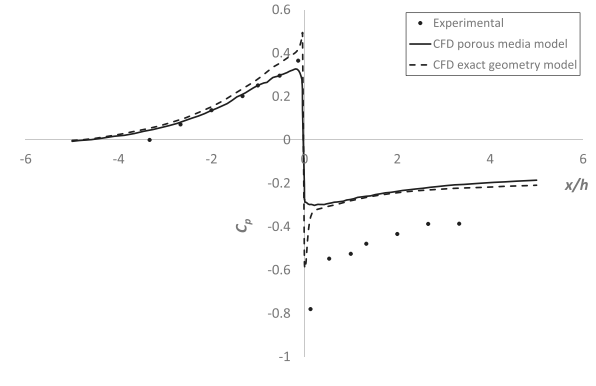
4. Conclusions

In this study, empirical formulae for determining the inertial and viscous resistance coefficients of the porous media model was presented. The results of the formulae were validated using experimental velocity values from PIV and pressure measurements. Validation was performed
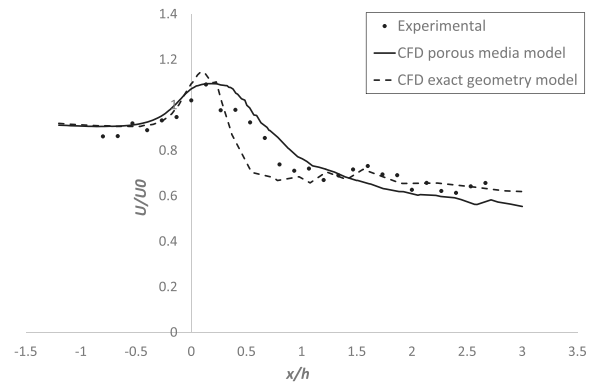
(a)
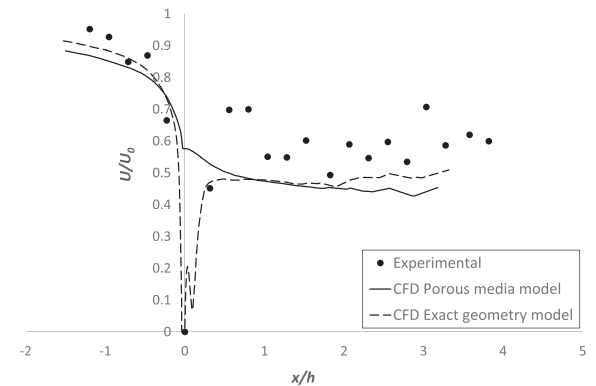
(b)

(c)

Fig. 21. Comparison between experimental, CFD of exact 3D geometry and porous media model results for the streamwise variation of velocity magnitude U/U_0 at (a) height $y/h = 1.2$ and (b) height $y/h = 0.8$ and (c) pressure coefficient C_p – Porosity ratio $\phi = 0.5$.

by comparing the results obtained using the porous media models to results from CFD of the exact geometry. For obtaining experimental results, six models with different porosity ratios, ranging from $\phi = 0.25$ to 0.6, were tested.

A parametric study was performed to observe the variation in pressure and velocity fields with inertial and viscous coefficients. The parametric study showed that the pressure drop relation is quadratic with viscous resistance and linear with inertial resistance. Whereas the velocity variation relation was quadratic when varying the inertial or viscous resistance coefficients.

Six models of different viscous and inertial resistance coefficients values were simulated using the porous media model. The CFD results were compared against PIV and experimental pressure measurements. A

Table 9

Comparison of the porous media model results with results from experiments and the CFD for the exact geometry – Porosity ratio $\phi = 0.5$.

	Exact geometry CFD					Experiments				
	Err.	FB	MG	VG	R	Err.	FB	MG	VG	R
U/U_0 at $y/h = 1.2$	10.5%	−0.05	0.958	1.017	0.906	6.4%	−0.016	0.992	1.005	0.78
U/U_0 at $y/h = 0.8$	5.5%	0.027	1.028	1.0056	0.78	19.8%	0.184	1.206	1.06	0.66
C_p	12%	−0.114	1.114	1.03	0.969	26%	1.24	1.34	1.24	0.97

correlation between the velocity drop for either the viscous and the inertial resistances was obtained. The correlation was used to obtain a relationship between the porosity ratio and the empirical coefficients.

For model validation, the results from the porous media model were compared against CFD for the exact geometry and experimental results. The validation showed that the porous media model yielded an average error of 6% in the velocity magnitude value. The comparison with the velocity values from the CFD of the exact geometry yielded an average error of 8%. The comparison with experimental pressure measurement yielded less agreement with porous media model. However, the comparison with the results of CFD of the exact geometry showed better agreement than experiments, with an average absolute error of 12%.

The results show that the porous media model is successfully able to capture the general characteristics of the flow through the exact geometry, however the details of the flow are not captured. Moreover, the pressure drop results showed less agreement than velocity magnitude. This also indicates that the porous media model is not suitable as a stand alone model to study geometries with perforation with acceptable accuracy. However, it can be used to model the effect of the presence of porous fences in a more complex geometry (for example urban areas) to avoid the necessity of modeling the exact geometry when performing numerical simulations.

The applicability of the formulae in this paper is limited to perforated surfaces with porosity ratios in the range from 0.25 to 0.6. For future work, further improvement can produce formulae that are applicable for a wider range of porosity values, vegetation barriers and other porous fences configurations. Empirical formulae similar to the ones obtained in this study can be formulated to obtain the resistance coefficients needed to model vegetation barriers using the porous media model. However, differently from perforated surfaces studied in this article, trees need to be modeled as an isotropic porous media.

Declaration of Competing Interest

The authors report no declarations of interest.

Acknowledgments

References

Adamek, K., Vasan, N., Elshaer, A., English, E., & Bitsuamlak, G. (2017). Pedestrian level wind assessment through city development: A study of the financial district in Toronto. *Sustainable Cities and Society, 35*, 178–190. https://doi.org/10.1016/j.scs.2017.06.004

ANSYS Inc. (2013). *ANSYS Fluent User' s Guide Release 15.0*. Canonsburg, Pennsylvania: ANSYS, Inc.

Arya, S., Novak, T., Saito, K., Levy, A., & Sottile, J. (2019). Empirical Formulae for Determining Pressure Drop Across a 20-Layer Flooded-Bed Scrubber Screen. *Mining, Metallurgy and Exploration*. https://doi.org/10.1007/s42461-019-0091-5

Bejan, A., Dincer, I., Lorente, S., Miguel, A. F., & Reis, A. H. (2004). *Porous and complex flow structures in modern technologies* (Vol. 66). https://doi.org/10.1007/978-1-4757-4221-3

Bitog, J. P., Lee, I. B., Hwang, H. S., Shin, M. H., Hong, S. W., Seo, I. H., et al. (2011). A wind tunnel study on aerodynamic porosity and windbreak drag. *Forest Science and Technology, 7*, 8–16. https://doi.org/10.1080/21580103.2011.559939

Breugem, W. P., Boersma, B. J., & Uittenbogaard, R. E. (2006). The influence of wall permeability on turbulent channel flow. *Journal of Fluid Mechanics, 562*, 35–72. https://doi.org/10.1017/S0022112006000887

Buccolieri, R., Santiago, J. L., Rivas, E., & Sanchez, B. (2018). Review on urban tree modelling in CFD simulations: Aerodynamic, deposition and thermal effects. *Urban Forestry and Urban Greening, 31*, 212–220. https://doi.org/10.1016/j.ufug.2018.03.003

Chang, J. C., & Hanna, S. R. (2004). Air quality model performance evaluation. *Meteorology and Atmospheric Physics, 87*, 167–196. https://doi.org/10.1007/s00703-003-0070-7

Cong, X. C., Cao, S. Q., Chen, Z. L., Peng, S. T., & Yang, S. L. (2011). Impact of the installation scenario of porous fences on wind-blown particle emission in open coal yards. *Atmospheric Environment, 45*, 5247–5253. https://doi.org/10.1016/j.atmosenv.2011.07.005

Dantec Dynamics. (2012). *Dynamic studio user's guide. Skovlunde*. Denmark: Dantec Dynamics.

Dong, Z., Luo, W., Qian, G., Lu, P., & Wang, H. (2010). A wind tunnel simulation of the turbulence fields behind upright porous wind fences. *Journal of Arid Environments, 74*, 193–207. https://doi.org/10.1016/j.jaridenv.2009.03.015

Dong, Z., Luo, W., Qian, G., & Wang, H. (2007). A wind tunnel simulation of the mean velocity fields behind upright porous fences. *Agricultural and Forest Meteorology, 146*, 82–93. https://doi.org/10.1016/j.agrformet.2007.05.009

Gan, G., & Riffat, S. B. (1997). Pressure loss characteristics of orifice and perforated plates. *Experimental Thermal and Fluid Science, 14*, 160–165. https://doi.org/10.1016/S0894-1777(96)00041-6

Ghani, S., El-Bialy, E. M. A. A., Bakochristou, F., Mohamed Rashwan, M., Mohamed Abdelhalim, A., Mohammad Ismail, S., et al. (2020). Experimental and numerical investigation of the thermal performance of evaporative cooled greenhouses in hot and arid climates. *Science and Technology for the Built Environment, 26*, 141–160. https://doi.org/10.1080/23744731.2019.1634421

Ghani, S., Gamaledin, S. M. A., Bakochristou, F., El-Bialy, E., Mohamed, M. M., & Elsawi, R. M. E. H. (2018). Numerical and wind tunnel investigation of hot air recirculation across liquefied natural gas air cooled heat exchangers. *Journal of Wind Engineering and Industrial Aerodynamics, 172*, 409–422. https://doi.org/10.1016/j.jweia.2017.11.026

Gromke, C. (2018). Wind tunnel model of the forest and its Reynolds number sensitivity. *Journal of Wind Engineering and Industrial Aerodynamics, 175*, 53–64. https://doi.org/10.1016/j.jweia.2018.01.036

Guo, B. Y., Hou, Q. F., Yu, A. B., Li, L. F., & Guo, J. (2013). Numerical modelling of the gas flow through perforated plates. *Chemical Engineering Research and Design, 91*, 403–408. https://doi.org/10.1016/j.cherd.2012.10.004

He, S., Zhang, G., Gao, M., Sun, F., & Huang, X. (2019). Wind tunnel test on the flow resistance of U-type water collecting devices for natural draft wet cooling towers. *Journal of Wind Engineering and Industrial Aerodynamics, 186*, 234–240. https://doi.org/10.1016/j.jweia.2019.01.008

Heisler, G. M., & Dewalle, D. R. (1988). 2 Effects of windbreak structure on wind flow. *Agriculture, Ecosystems and Environment, 22–23*, 41–69. https://doi.org/10.1016/0167-8809(88)90007-2

Hu, Z., Yu, B., Chen, Z., Li, T., & Liu, M. (2012). Numerical investigation on the urban heat island in an entire city with an urban porous media model. *Atmospheric Environment, 47*, 509–518. https://doi.org/10.1016/j.atmosenv.2011.09.064

Joseph, D. D., Nield, D. A., & Papanicolaou, G. (1982). Nonlinear equation governing flow in a saturated porous medium. *Water Resources Research, 18*, 1049–1052. https://doi.org/10.1029/WR018i004p01049

Kang, G., Kim, J. J., & Choi, W. (2020). Computational fluid dynamics simulation of tree effects on pedestrian wind comfort in an urban area. *Sustainable Cities and Society, 56*, 102086. https://doi.org/10.1016/j.scs.2020.102086

Kemper, F. H., & Feldmann, M. (2019). Wind load assumptions for permeable cladding elements considering the installation context. *Journal of Wind Engineering and Industrial Aerodynamics, 184*, 277–288. https://doi.org/10.1016/j.jweia.2018.10.011

Kent, C. W., Grimmond, S., & Gatey, D. (2017). Aerodynamic roughness parameters in cities: Inclusion of vegetation. *Journal of Wind Engineering and Industrial Aerodynamics, 169*, 168–176. https://doi.org/10.1016/j.jweia.2017.07.016

Kozmar, H., Procino, L., Bartoli, G., & Borsani, A. (2009). Wind barriers on bridges: Effects of wind incidence angle on flow field characteristics. *Mechanical engineering 1995*. Taipei, Taiwan.

Lage, J. (1998). *The fundamental theory of flow through permeable Mdeia from Darcy to turbulence*. Elsevier Science Ltd.. https://doi.org/10.1016/b978-008042843-7/50001-5

Lee, S. J., & Kim, H. B. (1999). Laboratory measurements of velocity and turbulence field behind porous fences. *Journal of Wind Engineering and Industrial Aerodynamics, 80*, 311–326. https://doi.org/10.1016/S0167-6105(98)00193-7

Lee, S. J., & Lim, H. C. (2001). A numerical study on flow around a triangular prism located behind a porous fence. *Fluid Dynamics Research, 28*, 209–221. https://doi.org/10.1016/S0169-5983(00)00030-7

Lee, S. J., Park, K. C., & Park, C. W. (2002). Wind tunnel observations about the shelter effect of porous fences on the sand particle movements. *Atmospheric Environment, 36*, 1453–1463. https://doi.org/10.1016/S1352-2310(01)00578-7

Liu, B., Qu, J., Zhang, W., Tan, L., & Gao, Y. (2014). Numerical evaluation of the scale problem on the wind flow of a windbreak. *Scientific Reports, 4*, 20–22. https://doi.org/10.1038/srep06619

Mahgoub, A. O., Ghani, S., Rashwan, M. M., Ismail, S. M., & ElBialy, E. A. (2020). Simulation of spectators' aerodynamic drag using porous models approximation. *Building and Environment, 184*, 107248. https://doi.org/10.1016/j.buildenv.2020.107248

Minoru, N., Shintarou, T., Koumei, A., & Fumiaki, N. (2014). Decision method of pressure loss coefficient of windbreak nets For CFD. *Proceedings of National Symposium on Wind Engineering, 23*, 445. https://doi.org/10.14887/kazekosymp.23.0_445

Nowak, R. (2016). Estimation of viscous and inertial resistance coefficients for various heat sink configurations. *Procedia Engineering*. https://doi.org/10.1016/j.proeng.2016.08.347

Özahi, E. (2015). An analysis on the pressure loss through perforated plates at moderate Reynolds numbers in turbulent flow regime. *Flow Measurement and Instrumentation, 43*, 6–13. https://doi.org/10.1016/j.flowmeasinst.2015.03.002

Patton, E. G., Shaw, R. H., & Judd, M. J. (1998). Large-Eddy simulation of windbreak flow. *Boundary-Layer Meteorology*, 275–306.

Perry, R. H., & Green, D. W. (2008). *Perry's chemical engineers' handbook* (8th ed.). New York: McGraw-Hill.

Procino, L., Kozmar, H., Bartoli, G., & Borsani, A. (2008). Wind barriers on bridges: the effect of wall porosity. *Mechanical engineering 14*, 20–24.

Raupach, M. R., Woods, N., Dorr, G., Leys, J. F., & Cleugh, H. A. (2001). The entrapment of particles by windbreaks. *Atmospheric Environment, 35*, 3373–3383. https://doi.org/10.1016/S1352-2310(01)00139-X

Reynolds, A. J. (1969). Flow deflection by gauze screens. *Journal of Mechanical Engineering Science, 11*, 290–294. https://doi.org/10.1243/JMES_JOUR_1969_011_036_02

Rosti, M. E., Brandt, L., & Pinelli, A. (2018). Turbulent channel flow over an anisotropic porous wall – Drag increase and reduction. *Journal of Fluid Mechanics, 842*, 381–394. https://doi.org/10.1017/jfm.2018.152. arXiv:1802.00477

Santiago, J. L., Buccolieri, R., Rivas, E., Calvete-Sogo, H., Sanchez, B., Martilli, A., et al. (2019). CFD modelling of vegetation barrier effects on the reduction of traffic-related pollutant concentration in an avenue of Pamplona, Spain. *Sustainable Cities and Society, 48*, 101559. https://doi.org/10.1016/j.scs.2019.101559

Santiago, J. L., Martín, F., Cuerva, A., Bezdenejnykh, N., & Sanz-Andrés, A. (2007). Experimental and numerical study of wind flow behind windbreaks. *Atmospheric Environment, 41*, 6406–6420. https://doi.org/10.1016/j.atmosenv.2007.01.014

Slinn, W. G. (1982). Predictions for particle deposition to vegetative canopies. *Atmospheric Environment, 16*, 1785–1794. https://doi.org/10.1016/0004-6981(82)90271-2

Soper, D., Gillmeier, S., Baker, C., Morgan, T., & Vojnovic, L. (2019). Aerodynamic forces on railway acoustic barriers. *Journal of Wind Engineering and Industrial Aerodynamics, 191*, 266–278. https://doi.org/10.1016/j.jweia.2019.06.009

Wang, H., Takle, E. S., & Shen, J. (2001). Shelterbelts and windbreaks: mathematical modeling and computer simulations of turbulent flows. *Annual Review of Fluid Mechanics, 33*, 549–586. https://doi.org/10.1146/annurev.fluid.33.1.549

Wilson, J. D. (1987). On the choice of a windbreak porosity profile. *Boundary-Layer Meteorology*.

Wilson, J. D. (1997). A field study of the mean pressure about a windbreak. *Boundary-Layer Meteorology, 85*, 327–358. https://doi.org/10.1023/A:1000582917218

Zeng, F., Lei, C., Liu, J., Niu, J., & Gao, N. (2020). CFD simulation of the drag effect of urban trees: Source term modification method revisited at the tree scale. *Sustainable Cities and Society, 56*. https://doi.org/10.1016/j.scs.2020.102079

Zheng, S., Guldmann, J. M., Liu, Z., Zhao, L., Wang, J., Pan, X., et al. (2020). Predicting the influence of subtropical trees on urban wind through wind tunnel tests and numerical simulations. *Sustainable Cities and Society, 57*, 102116. https://doi.org/10.1016/j.scs.2020.102116